Received: 6 September 2022 | Revised: 21 October 2022 | Accepted: 22 October 2022

DOI: 10.1111/ijac.14265

International Journal of Applied Ceramic Technology

SPECIAL ISSUE ARTICLE

Thermal properties of field-assisted-sintered SiCN–Y_2O_3 composites

Zhao Zhang[1] | **Quan Li**[1,2] | **Sanat Chandra Maiti**[1,3] | **Xingchen Shen**[4] | **Jian He**[5] | **Fei Peng**[1] | **Ranjendra K. Bordia**[1]

[1]Department of Materials Science and Engineering, Clemson University, Clemson, South Carolina, USA

[2]College of Materials Science and Engineering, Nanjing Tech University, Nanjing, China

[3]College of Materials Science and Engineering, GE Research, Bengaluru, India

[4]College of Physics, Chongqing University, Chongqing, P. R. China

[5]Department of Physics and Astronomy, Clemson University, Clemson, South Carolina, USA

Correspondence
Fei Peng and Rajendra K. Bordia, Department of Materials Science and Engineering, Clemson University, Clemson, SC 29634, USA.
Email: fpeng@clemson.edu and rbordia@clemson.edu

Funding information
US Department of Energy, National Energy Technology Lab, Grant/Award Number: DE-FE003128; GE Gas Power; National Science Foundation EPSCoR Program, Grant/Award Number: # OIA-1655740

Abstract

Polymer-derived amorphous SiCN has excellent high-temperature stability and properties. To reduce the shrinkage during pyrolysis and to improve the high-temperature oxidation resistance, Y_2O_3 was added as a filler. In this study, polymer-derived SiCN–Y_2O_3 composites were fabricated by mixing a polymeric precursor of SiCN with Y_2O_3 submicron powders in different ratios. The mixtures were cross-linked and pyrolyzed in argon. SiCN–Y_2O_3 composites were processed using field-assisted sintering technology at 1350°C for 5 min under vacuum. Dense SiCN–Y_2O_3 composite pellets were successfully made with relative density higher than 98% and homogeneous microstructure. Due to low temperature and short time of the heat-treatment, the grain growth of Y_2O_3 was substantially inhibited. The Y_2O_3 grain size was ~1 μm after sintering. The composites' heat capacity, thermal diffusivity, and thermal expansion coefficients were characterized as a function of temperature. The thermal conductivity of the composites ceramics decreased as the amount of amorphous SiCN increased and the coefficient of thermal expansion (CTE) of the composites increased with Y_2O_3 content. However, the thermal conductivity and CTE did not follow the rule of mixture. This is likely due to the partial oxidation of SiCN and the resultant impurity phases such as Y_2SiO_5, $Y_2Si_2O_7$, and $Y_{4.67}(SiO_4)_3O$.

KEYWORDS
composites, field-assisted sintering technology (FAST), polymer precursor, thermal properties

1 | INTRODUCTION

Polymer-derived ceramics (PDCs) are a class of ceramics that are made by the conversion of a polymer into the ceramic phase.[1] They are used to produce various kinds of ceramics, including SiC, SiCN, SiCO, Si_3N_4, BN, SiO_2.[2,3] Polymer-derived SiCN is attractive because of its high-temperature stability, and mechanical and electronic properties. They have potential applications as catalyst support,[4] optoelectronics UV detectors,[5] microelectromechanical systems,[6] and high-temperature materials from electromagnetic shielding.[7] One outstanding feature of

polymer-derived SiCNs is that they can be amorphous up to 1500°C.[2,8] This feature helps the material avoid grain-boundary-limited properties, such as grain growth and creep. However, although SiCN has excellent high-temperature oxidation resistance behavior in dry air, its oxidation resistance is limited in an environment with both oxygen and steam due to the reaction of the SiO_2 layer and water vapor leading to formation of volatile species.[9,10] This results in active oxidation with weight loss and surface recession.

One significant disadvantage of PDCs is the high shrinkage during the polymer-to-ceramic conversion—as much as 60%–80% volumetric shrinkage.[2,11] For bulk components, this large shrinkage leads to high porosity and/or cracks.[3,12] For coatings, the large shrinkage leads to cracking due to constrained shrinkage and limits the thickness of crack-free coatings to a few microns.[13] One way to compensate for the high shrinkage is to introduce activate or passive filler into the preceramic precursor.[12,14] Active fillers react with solid or gaseous decomposition products, leading to formation of carbides, nitrides, or oxides during pyrolysis. The volume expansion caused by the carburization, nitridation, or oxidation can compensate for the polymer shrinkage.[14] Another strategy to control the shrinkage during the polymer–ceramic transition is to use inert fillers, which do not participate in the chemical reaction during the pyrolysis but reduce the shrinkage by reducing the volume fraction of the polymer. Both of these strategies have been used to make low shrinkage bulk composites[15] and crack-free thick environmental barrier coatings.[13,16–20]

Yttrium oxide is a highly refractory material with excellent corrosion resistance. By adding Y_2O_3 powder into SiCN precursors, under the right conditions Y_2O_3 reacts with the SiO_2 (due to oxidation of SiCN) and forms yttrium silicates.[21,22] Yttrium silicates, with their excellent mechanical properties, low oxygen permeability, high stability in water vapor, and high melting point, have been shown to reduce the oxidative degradation of C, SiC, and Si_3N_4.[21–26]

The densification of SiCN is challenging and requires high temperature.[27] Similarly, the densification of Y_2O_3 requires high temperature (>1800°C) and a long soaking time.[28] In addition, due to the well-known challenges in sintering of composites,[29] sintering of SiCN–Y_2O_3 composites is a challenge. One promising approach is field-assisted sintering technology (FAST) (also called spark plasma sintering).[29,30] In this technique, instead of using an external heating source, electrodes are connected to a graphite die. Pressure and pulsed current are applied to the punches leading to direct Joule heating of the die and the sample. Compared to typical heating rate in conventional sintering (e.g., 10–20°C/min), the heating rate of FAST can be as high as 100–1000°C/min. Because of the high heating rate, shorter dwell time, and applied pressure, rapid sintering is realized with limited grain growth, FAST has become an attractive technique especially for hard-to-sinter materials like carbides, nitrides, and composites.[30–32] It has also been used to densify Y_2O_3[33] and polymer-derived ceramics.[34]

In this study, we show that dense SiCN–Y_2O_3 composites can be fabricated by FAST. In addition, the temperature and composition dependence of their thermal properties are reported. Polymer-derived amorphous SiCN and Y_2O_3 powders were used as the starting raw materials.

2 | EXPERIMENTAL PROCEDURES

FAST with high heating rates was employed to prepare SiCN–Y_2O_3 composites. The schematic configuration is shown in Figure 1. The effects of composition and processing temperatures on microstructure, phases, thermal, and thermomechanical properties of the composites were investigated and are reported in this paper.

The process flow diagram is shown in Figure 2. Four compositions of SiCN–Y_2O_3 composite powders based on different SiCN:Y_2O_3 volume ratio were prepared. To obtain the composite powders, the corresponding slurries were first prepared. Dispersant Disperbyk-2070 (BYK, Wesel, Germany) was mixed thoroughly with di-*n*-butyl ether (Acros Organics, Pittsburg, USA). The quantity of the dispersant was 7.5 wt% of Y_2O_3 powders (American Elements, 99.9%, average particle size .5–1 μm). Based on the Y_2O_3–SiCN volume ratio, the corresponding mass of Y_2O_3 powder was then added to form the suspension. To achieve a well-dispersed suspension, high-energy ultrasonication (Vibra Cell VC-500, Sonics, CT, USA) was used for 2 h. Overall, 3 wt% DCP (dicumyl peroxide, Sigma-Aldrich Chemie GmbH, Germany), acting as initiator, was first dissolved in Durazane 1800 (Durazane 1800, Merck KGaA, Germany) using an ultrasonicator (VWR, Radnor, USA). The polysilazane with DCP was then added to the suspension in the flask and purged with flowing argon in a glove box during magnetic stirring. After mixing, the flask was transferred to a rotary evaporator running at 80°C for 5 h. The dried sample was first cross-linked at 400°C for 2 h and then pyrolyzed at 900°C for 2 h. These last two steps were conducted in a tube furnace under flowing argon. Pyrolyzed powders were milled in isopropanol in air for 60 h with zirconia balls in a planetary ball mill to obtain the submicron powders.

The pyrolysis and mass change behavior of the pure cross-linked Durazane powders was characterized using thermogravimetric analysis (TGA) (NETZSCH STA 449 F3 Jupiter) from room temperature to 1100°C at a rate

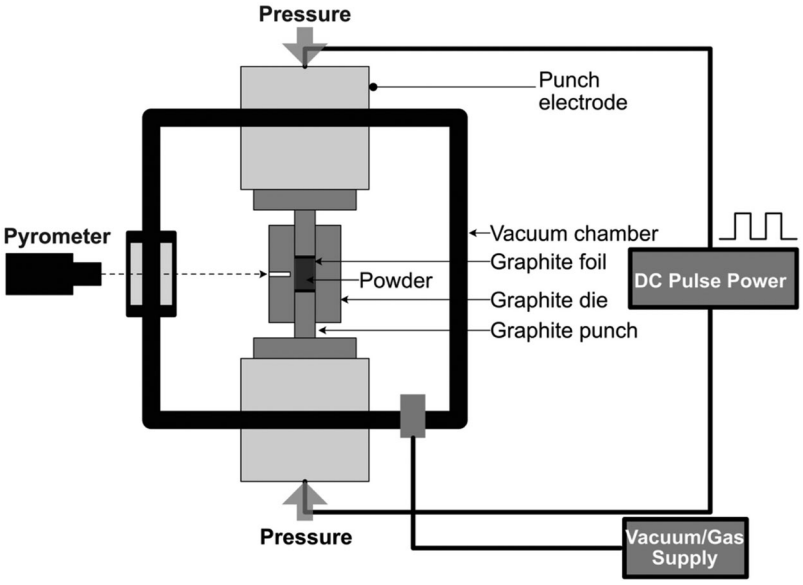

FIGURE 1 FAST sintering experimental set-up

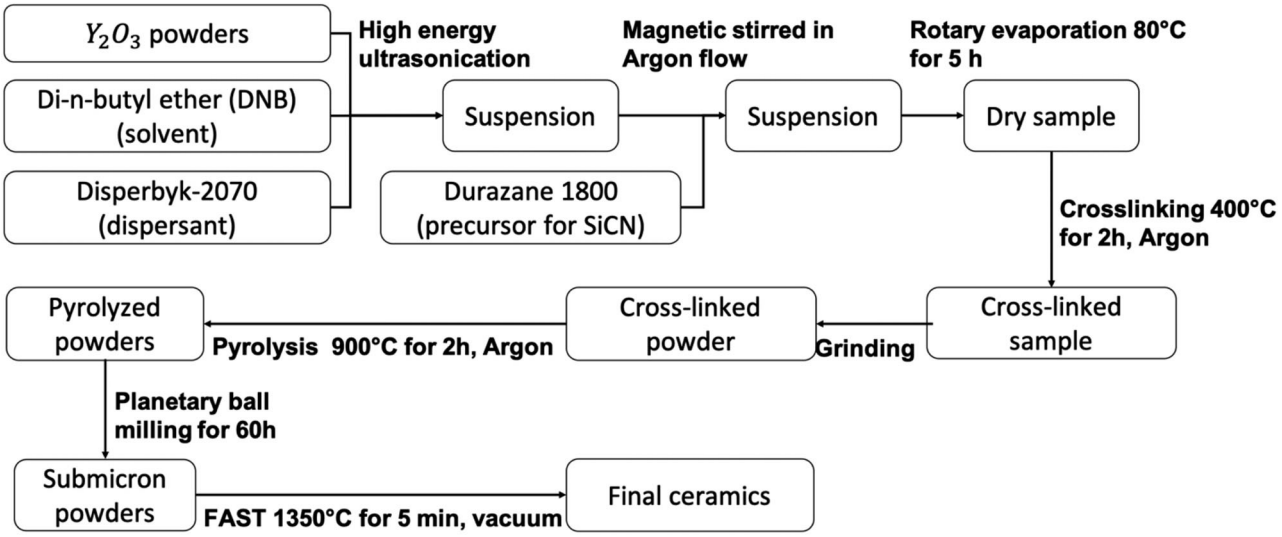

FIGURE 2 Process flow diagram for making the composites

of 2.5°C/min under argon atmosphere. The mass conversion rate of pure Durazane was calculated based on weight change before and after crosslinking using an analytical balance (PI-214, Denver Instrument Co., Denver, CO).

To sinter the sample by the FAST technique, the powders were filled into a 32 mm diameter graphite die with a hole of 10 mm drilled through the center of the die. Two pieces of graphite foils were placed between powders and graphite punches to facilitate demolding after FAST processing. Graphite foil was also used to wrap the inner surface of the graphite die. By doing so, the gap between the graphite dies and punches was sealed, protecting the die from contamination. During the FAST process, a constant axial compressive stress of 20 MPa was applied through the punches of the FAST system (Dr. Sinter-1020, Sumitomo Coal Mining Co.). An increasing AC current (50 A/min) starting from 250 A was applied simultaneously to the die in a dynamic vacuum (~6 Pa), whereas the temperature of the sample was monitored by a pyrometer. The heating rate was around 150°C/min. Samples were held at the target temperature (1250 or 1350°C) for 5 min before AC current was shut off.

For the sintered samples, the thermal conductivity was calculated based on the relationship: $\kappa = DC_P\rho$, where κ is the thermal conductivity, D is the thermal diffusivity, C_P is the heat capacity, and ρ is the density. Thermal diffusivity was measured using the laser flash diffusivity method (NETZSCH LFA 457 Netzsch, Selb, Germany) from 25 to 600°C. The heat capacity was calorimetrically measured from 25 to 600°C (NETZSCH DSC 404C) (Netzsch,

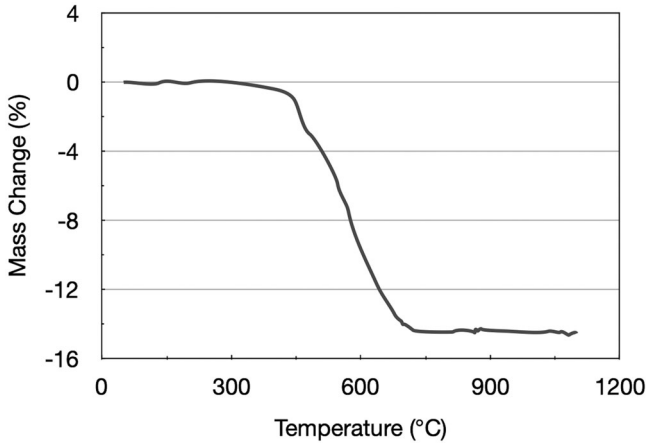

FIGURE 3 Thermogravimetric analysis (TGA) of the cross-linked Durazane powders up to 1100°C with a heating rate of 2.5°C/min under flowing argon atmosphere

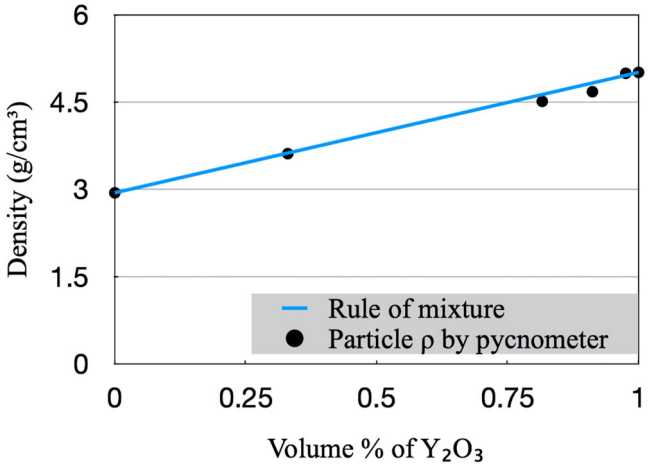

FIGURE 4 For the SiCN–Y_2O_3 composites, the theoretical density (calculated using rule of mixtures) and experimental density (measured using pycnometer), as a function of Y_2O_3 volume percentage

Selb, Germany). Sample density was measured using the Archimedes method.

Linear thermal expansion coefficient (CTE) was measured using a computer-controlled horizontal pushrod dilatometer (NETZSCH 402C) (Netzsch, Selb, Germany) with a high-resolution displacement transducer. The specimens were placed in contact with the pushrod and heated to 1200°C at a rate of 10°C/min under ultrahigh purity Ar flow.

X-ray diffraction was used to analyze and identify the crystalline phases in the sintered samples (Rigaku MiniFlex 600) powder diffractometer (XRD), Rigaku MiniFlex 600 X-ray generator, Cu K_α radiation, $\lambda = 1.5406$ Å). Data were digitally recorded in a continuous scan in the range of angle (2θ) from 15° to 80° with a scanning rate of 1°/min.

The samples FAST sintered at 1350°C were polished and thermally etched under argon at 1200°C for 30 min in a tube furnace. The microstructures of the polished etched samples were observed by scanning electron microscopy (Hitachi S4800, Hitachi, Ltd., Tokyo, Japan).

3 | RESULTS

The thermal transformation of the cross-linked Durazane powders was characterized by TGA in argon at a temperature up to 1100°C with a heating rate of 2.5°C/min. The TGA result (Figure 3) shows that the total weight loss was approximately 14.5%. After crosslinking, there was almost no weight loss up to 400°C. Almost all the weight loss is between 400 and 700°C. Durazane loses a total of approximately 22.6% weight during crosslinking and pyrolysis in argon. Therefore, the total ceramic yield of Durazane 1800 after crosslinking and pyrolysis was 77.4%.

TABLE 1 Theoretical volume percentage of SiCN and Y_2O_3 in the composites

Sample name	Volume % of Y_2O_3	Volume % of SiCN
PY	100	0
Y2S	98	2
Y9S	91	9
Y18S	82	18
Y67S	33	67
PS	0	100

3.1 | Density

The particle densities measured by pycnometer (Figure 4) were compared to the theoretical density of the composites calculated using the rule of mixtures.[35] The measured density of all compositions matches the rule of mixture values. The particle density of pure SiCN is 2.94 g/cm^3, which is lower than both crystalline SiC (3.21 g/cm^3) and Si_3N_4 (3.17 g/cm^3). However, some studies found that the density of amorphous SiC and Si_3N_4 depends on the preparation pathways.[36,37] When in the amorphous phase, the density of SiC can be more than 12% lower than that in the crystalline phase (3.21 g/cm^3).37 Kroll[36] investigated amorphous Si_3N_4 using a density-functional method, and the model resulted in two structures for amorphous Si_3N_4 with densities of 3.06 and 2.60 g/cm^3. The density of amorphous PDC-SiCN agrees with the reported values mentioned before.

Based on the TGA and density results, we calculated the volume percentage of Y_2O_3 and SiCN after the pyrolysis for all the composites (Table 1).

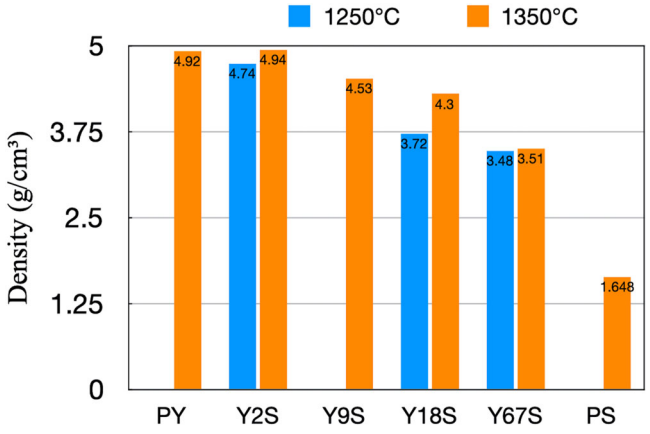

FIGURE 5 Bulk density of the SiCN–Y_2O_3 composites, measured using the Archimedes method, after field-assisted sintering technology (FAST) at 1250 and 1350°C for 5 min

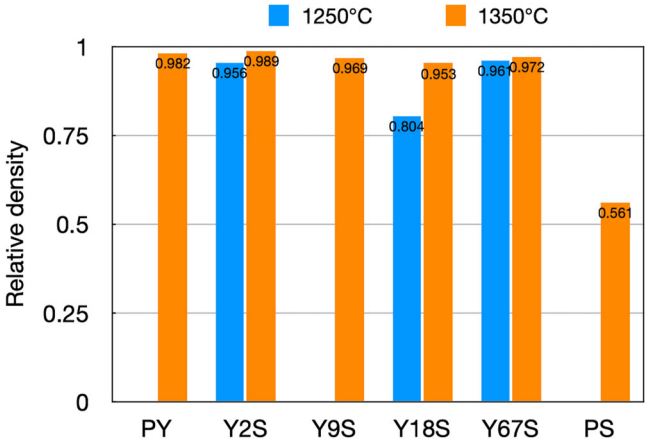

FIGURE 6 Relative density of the SiCN–Y_2O_3 composites, measured using the Archimedes method, after field-assisted sintering technology (FAST) at 1250 and 1350°C for 5 min

Increasing the FAST temperature from 1250 to 1350°C leads to a remarkable increase in sintered density. For Y2S, FAST processed at 1350°C, the density (4.94 g/cm^3) was very close to the theoretical density of pure Y_2O_3. Sample densities increased with the volume ratio of Y_2O_3. This is because of the higher theoretical density of Y_2O_3 (5.01 g/cm^3) compared with that of the amorphous SiCN (2.94 g/cm^3). Using the theoretical densities (Figure 4), the relative densities of the composites are calculated and are presented in Figure 5. All compositions reach high relative density, especially at 1350°C, except pure SiCN sample.

3.2 | Phase characterization

The phase composition of FAST sintered samples at 1350°C for 5 min is identified using XRD (Figure 6). XRD results show there was some oxidation of the SiCN. For samples Y2S and Y9S, only a small degree of oxidation occurs resulting in some Y_2SiO_5 due to the reaction of Y_2O_3 with SiO_2. With a higher content of SiCN, more oxidation was observed. No SiC or Si_3N_4 diffraction peaks were found. This is because amorphous PDC-SiCN is stable up to 1500°C.[38] For Y18S, the crystalline phases were Y_2O_3, Y_2SiO_5, and $Y_8Si_4N_4O_{14}$. When the PDC-SiCN volume percentage is raised to 67%, the sintered pellets had the crystalline phases of Y_2O_3, Y_2SiO_5, $Y_2Si_2O_7$, and $Y_{4.67}(SiO_4)_3O$. These results are expected because, at high temperatures, Y_2O_3 reacts with SiCNO to form various yttrium silicates.[21,22]

Backscattered electron images of the Y67S FAST sintered sample (Figure 7) show two distinct regions. The darker area is primarily composed of Si, N, and C derived from Durazane. The brighter area is dominated by Y and O. The scarcities of O and Y in the area where more Si, N, and C appear show the predominant existence of SiCN amorphous phases with the yttrium silicates being minority phases due to limited oxidation of SICN.

3.3 | Microstructure

Scanning electron micrographs (Figure 8) show that the average grain sizes of all samples are in the submicron scale, which means grain growth has been inhibited in the FAST-processed samples. Further, all the samples exhibited a homogenous microstructure. For Y2S samples, closed pores are observed, consistent with the density data. With a higher volume content of SiCN, more amorphous phases filling the pores and boundaries between grains can be observed (Figure 8D,F). For Y67S, the sample is mainly composed of amorphous phase.

3.4 | Thermal conductivity

The thermal properties of these composites are important as one of their potential applications is as thermal and environmental barrier coatings. The specific heat capacity (C_P) of the SiCN–Y_2O_3 composites, as a function of temperature, is plotted in Figure 9. In literature, to the best of our knowledge, values of C_P of SiCN–Y_2O_3 composites have not been reported, except for pure Y_2O_3. It is shown that the C_P of all composites increases with increasing temperature. C_P of pure Y_2O_3 changes from .45 J/(g K) at room temperature to around .6 J/(g K) at 600°C. This is consistent with the reported value.[39,40] For the composites, at all temperatures, the C_P increases as the volume fraction of SiCN increases. For all temperatures, the C_P for PY, Y2S and Y9S are essentially equal (within experimental error).

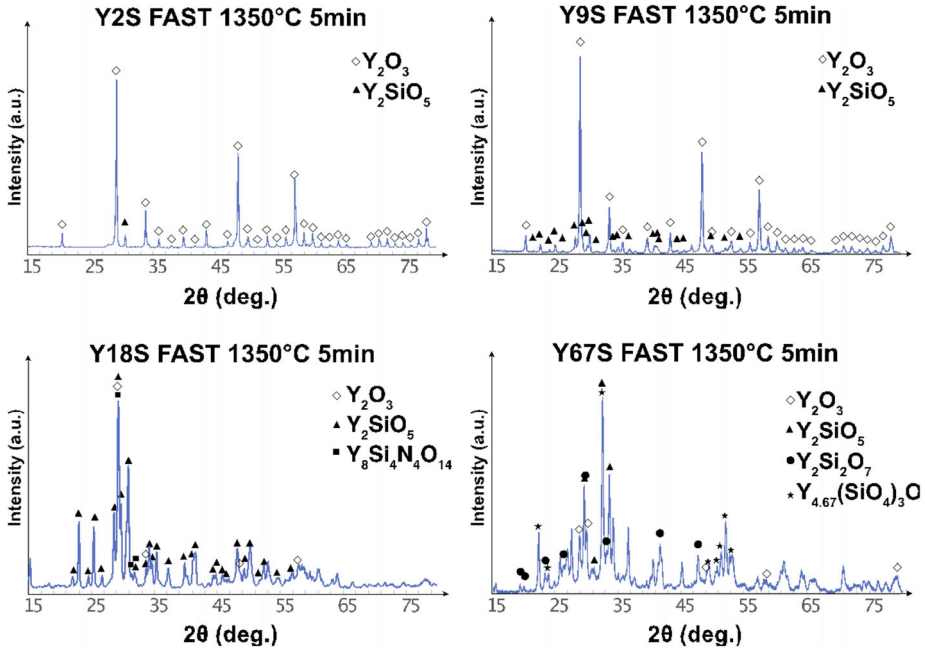

FIGURE 7 Crystalline phases in sintered SiCN–Y_2O_3 composites (field-assisted sintering technology [FAST] at 1350°C for 5 min under vacuum)

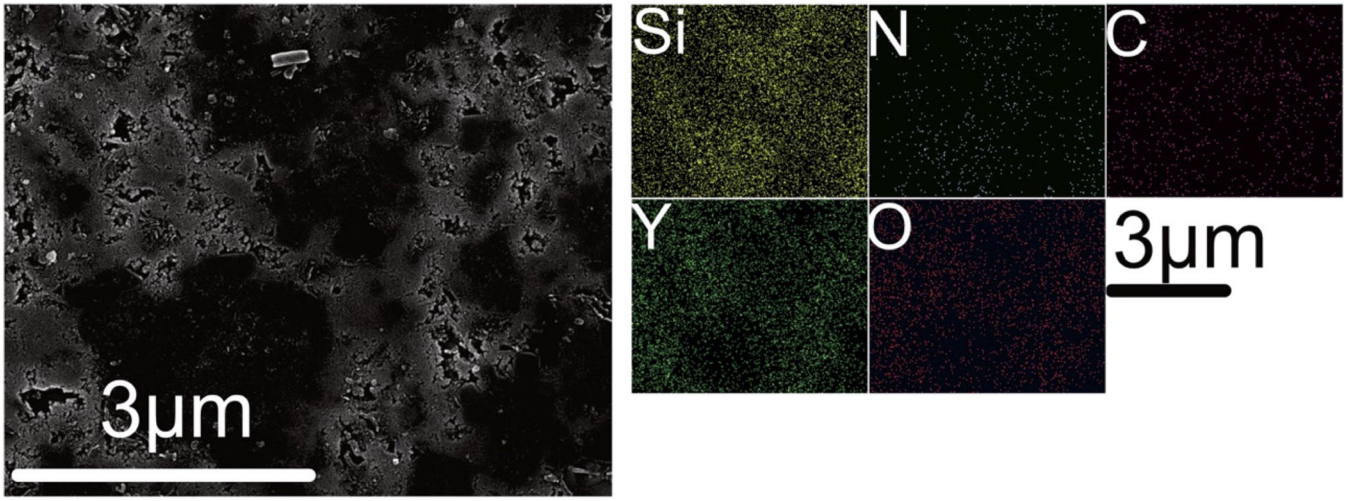

FIGURE 8 Backscattered electron images of sample Y67S field-assisted sintering technology (FAST) sintered at 1350°C for 5 min under vacuum

The measured thermal diffusivities of the investigated composites are plotted in Figure 10. The thermal diffusivity of all compositions decreases with temperature and the PDC content except for the composition Y67S that is higher than that for Y18S. The reason for this unusual behavior of this composite is not clears. The thermal conductivities calculated using $\kappa = DC_P\rho$, and experimental results of heat capacity (Figure 9) and density (Figure 11) are plotted in Figure 12. The results reflect the trends in thermal diffusivity (Figure 10).

3.5 | Coefficient of thermal expansion (CTE)

The average CTE of SiCN–Y_2O_3 composites (Table 2 and Figure 13) shows pure SiCN has the lowest value ($5.5 \pm .2 \times 10^{-6}$/K). Pure Y_2O_3 has a value of $8.7 \pm .1 \times 10^{-6}$/K. This is a similar value to the reported data.[41] Sample Y67S also had the expected value of CTE, approximately following the rule of mixtures and falling between Y_2O_3 and SiCN. However, for higher Y_2O_3

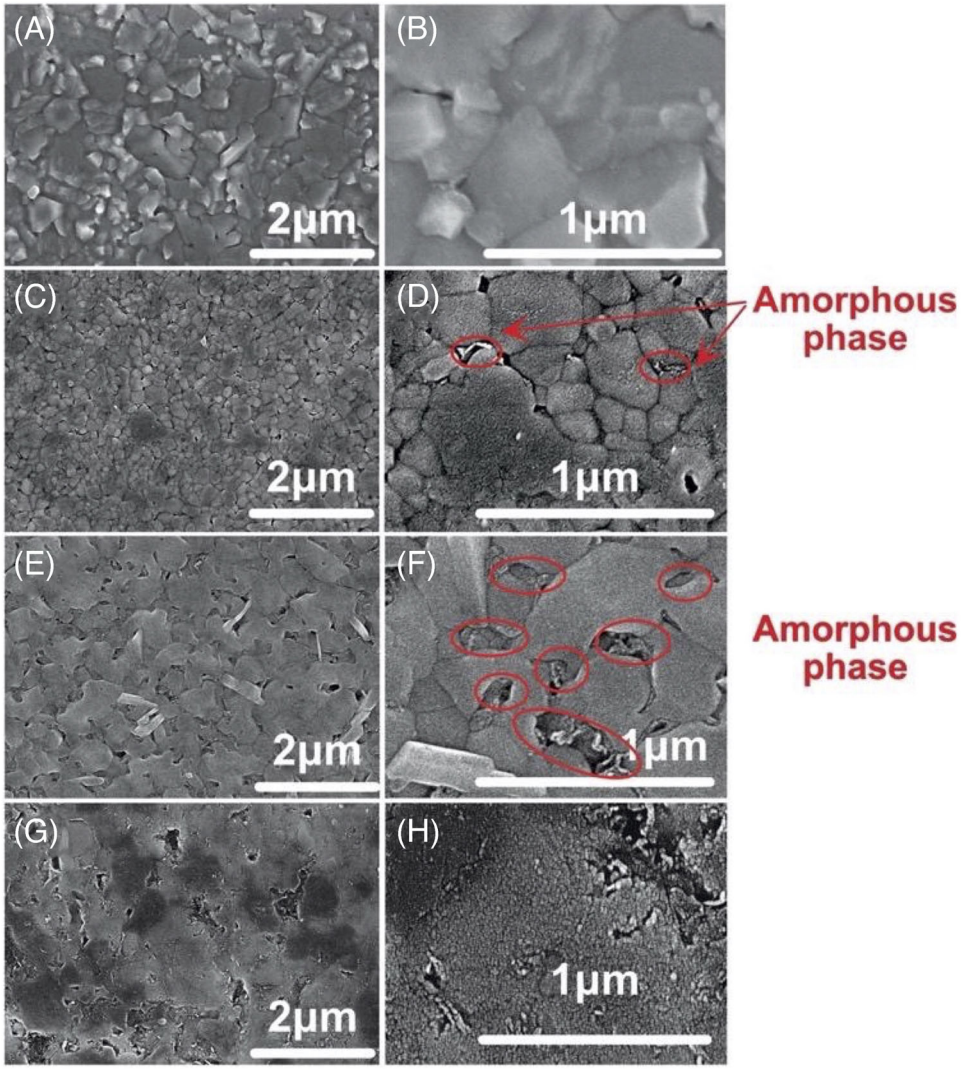

FIGURE 9 Microstructure of different samples field-assisted sintering technology (FAST) processed at 1350°C for 5 min under vacuum. Parts (A) and (B) are from Y2S sample; parts (C) and (D) are from Y9S sample; parts (E) and (F) are from Y18S; and parts (G) and (H) are from Y67S.

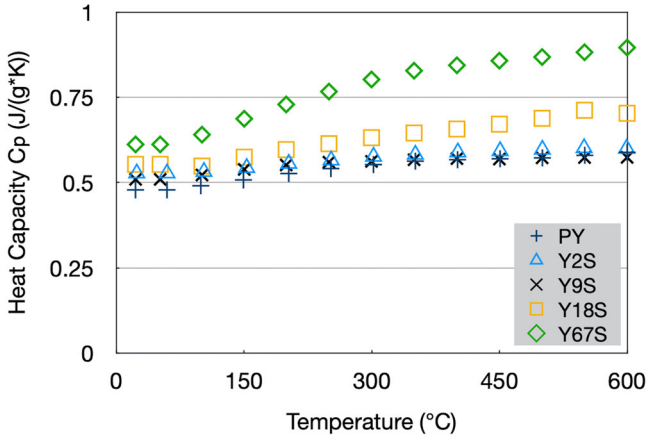

FIGURE 10 The heat capacity of SiCN–Y_2O_3 composites as a function of temperature and composition

content samples (Y2S, Y9S, Y18S), the measured CTE values are higher than both pure Y_2O_3 and pure SiCN. One possible reason is the oxidation of amorphous SiCN phases or other chemical reactions in these higher Y_2O_3 content composites during CTE measurements, thereby altering their CTE. It should be noted that the CTE measurements were conducted in air during cooling after heating to 1200°C. Further study is needed, especially CTE measurements in inert environment.

4 | DISCUSSION

SiCN–Y_2O_3 composites were sintered to high density at 1350°C for 5 min without anyy sintering aid while

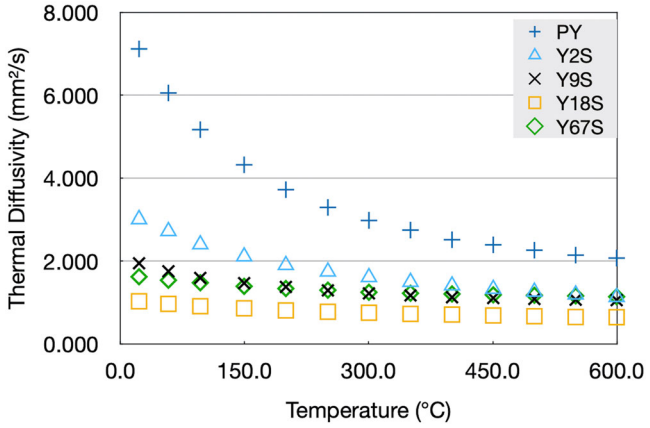

FIGURE 11 The thermal diffusivity of SiCN–Y_2O_3 composites as a function of temperature and composition

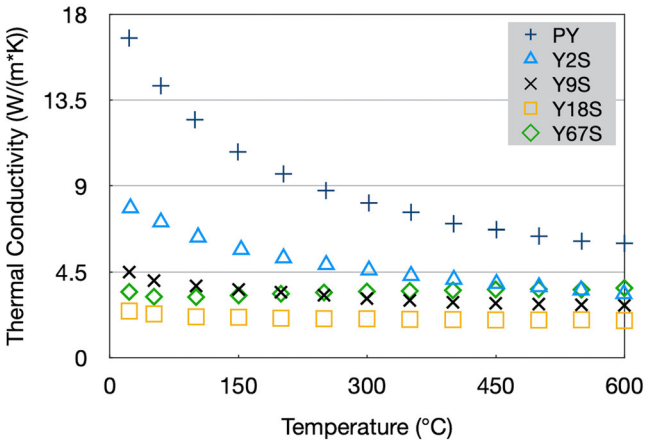

FIGURE 12 The thermal conductivity SiCN–Y_2O_3 composites as a function of temperature and composition

maintaining the micrometer scale grain sizes using FAST. The results show evidence of the well documented advantages of FAST in this system—ability to sinter composites to a high density in short time with limited grain growth. As an example, compared to the FAST sintering conditions, the fabrication of dense Y_2O_3 using conventional sintering methods typically requires temperature above 1700°C, holding for hours, and/or the need for sintering aids.[28,42] FAST has been recently applied to the sintering of dense, fine-grain Y_2O_3 at a much lower temperature and time.[33,43] During the FAST of Y_2O_3, the diffusion of yttrium cation along the grain boundary is the rate-controlling process.[33,43] Chaim et al.[33] found the improved sinterability of Y_2O_3 can be explained by the 3-order higher diffusion coefficient of yttrium cations in the grain boundary than the expected value for conventional sintering. The results of Yoshida et al.[43] indicated that the applied field during FAST enhanced the formation of defects (oxygen anion vacancies and interstitial yttrium

TABLE 2 Coefficient of thermal expansion (CTE) and main phases of SiCN–Y_2O_3 composites

Sample	Main phases	CTE ($\times 10^{-6}$/K)
PY	Y_2O_3	8.7 ± .1
Y2S	Y_2O_3, Y_2SiO_5, amorphous SiCN	10.0 ± .0
Y9S	Y_2O_3, Y_2SiO_5, amorphous SiCN	10.0 ± 1.4
Y18S	Y_2O_3, Y_2SiO_5, $Y_8Si_4N_4O_{14}$, amorphous SiCN	10.0 ± .4
Y67S	Y_2O_3, Y_2SiO_5, $Y_2Si_2O_7$, $Y_{4.67}(SiO_4)_3O$, amorphous SiCN	6.9 ± .5
PS	Amorphous SiCN	5.5 ± .2

Note: The identified phases are from the as processed composites (Figure 6).

cations) in the grain boundaries in Y_2O_3. Moreover thus, the matter transport in Y_2O_3 was accelerated. Besides, the fine-grain size (Figure 8) has the expected effect of fast densification due to the well-known effect of grain size on densification kinetics.[29]

When there is partial oxidation of SiCN, Y_2O_3 and amorphous SiCNO can form intergranular amorphous phases.[44–46] Wan et al.[46] found that when sintering amorphous SiCN(O) with Y_2O_3 as sintering additive, a higher amount of Y_2O_3 (8%) lowered the sintering temperature to 1300°C. This is consistent with our result: When no Y_2O_3 is added to amorphous SiCN powders, sample PS is poorly densified with a relative density of only 56%. However, addition of even small amount of Y_2O_3 significantly improves densification. During the FAST process, applied pressure also promotes densification.[47] Both higher pressure and sintering temperature increase the sintered density. However, higher sintering temperature leads to grain growth, which decreases the fracture of the ceramic.[48]

The observed phases can be explained by considering partial oxidation of SiCN according to

$$SiCN\,(s) + 2O_2\,(g) \rightarrow SiO_2\,(s) + CO\,(g) + NO\,(g) \quad (1)$$

The generated SiO_2 then can react with Y_2O_3 to form different yttrium silicates:

$$Y_2O_3\,(s) + SiO_2\,(s) \rightarrow Y_2SiO_5\,(s) \quad (2)$$

$$2.335Y_2O_3\,(s) + 3SiO_2\,(s) \rightarrow Y_{4.67}(SiO_4)_3O\,(s) \quad (3)$$

$$Y_2O_3\,(s) + 2SiO_2\,(s) \rightarrow Y_2Si_2O_7\,(s) \quad (4)$$

This stoichiometry ratio explains why with the increase of the amorphous SiCN phase content, yttrium silicate changes from Y_2SiO_5 to $Y_{4.67}(SiO_4)_3O$, and finally to

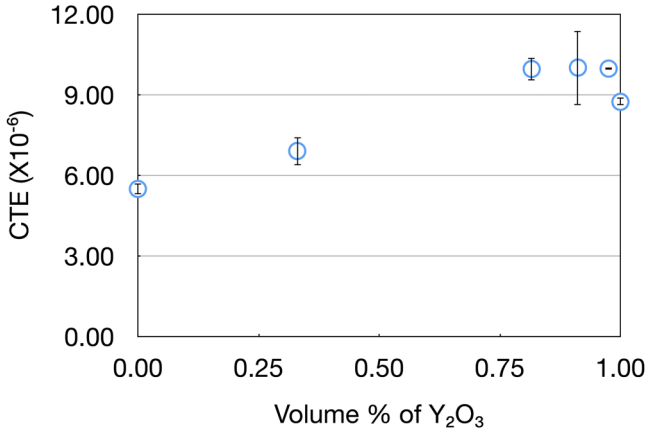

FIGURE 13 The average coefficient of thermal expansion for SiCN–Y_2O_3 composites in the range from 400 to 1200°C during cooling

TABLE 3 Reported Debye temperatures and thermal conductivities of the main phases[50,52,53]

	Y_2O_3	Y_2SiO_5	Y_2SiO_7	SiO_2
Debye *T* (K)		580	~577	470
Thermal conductivity (W/(m K))	7–15	1.5–1.6	3.5–	

$Y_2Si_2O_7$. Besides, according to reactions (5) and (6),[49,50] nitrogen-containing phases may also oxidize and generate $Y_4Si_2N_2O_7$. Subsequently, $Y_4Si_2N_2O_7$ reacts with oxygen and decomposes into $Y_{4.67}(SiO_4)_3O$ and Y_2O_3.

$$4Y_2O_3\,(s) + Si_3N_4\,(s) + SiO_2\,(s) = 2Y_4Si_2N_2O_7\,(s) \quad (5)$$

$$1.5Y_4Si_2N_2O_7\,(s) + 2.25O_2\,(g) \rightarrow Y_{4.67}(SiO_4)_3O\,(s) + 0.665Y_2O_3\,(s) + 1.5N_2\,(g) \quad (6)$$

Regarding thermal properties, above the Debye temperature, the heat capacities of a material can be considered constant.[51] The Debye temperatures of the main phases of composites are listed below in Table 3. Above 300°C, the heat capacities of PD, Y2S, and Y9S are almost constant (Figure 9). Based on the reported results,[50,52] the thermal conductivity of pure Y_2O_3 decreases from 15 to 7 W/(m K) in the range from room temperature to 600°C. Our results are consistent with these reported values. For composites Y2S, the main crystalline phase is Y_2O_3, which is why this composite possess the highest thermal conductivity. With Y_2O_3 content decreasing, more amorphous phases, along with the crystalline Y_2SiO_5 phase, appeared. Due to the low thermal conductivity of Y_2SiO_5 and other yttrium silicates,[53] the thermal conductivity of the composites decreases. Based on our XRD results, the composition Y18S has the highest content of Y_2SiO_5. This explains why Y18S has the lowest thermal conductivities of all four compositions. In addition, the amorphous phases also contribute to the thermal conductivity. Compared to crystalline phases, the thermal properties of the amorphous phase are less explored.[54] It has been shown that the thermal conductivity values of amorphous silicon nitride (SiN_x) and silicon carbide have a wide range (SiN_x: .7–13 W/(m K); SiC: .12–4.2 W/(m K)) depending on fabrication methods, sample dimensions, density, and mean free path vibrational modes.[54]

5 | CONCLUSION

High relative density SiCN–Y_2O_3 composites of various compositions were fabricated by FAST at 1350°C for 5 min under vacuum. The composites have a homogenous microstructure with a high relative density (~98%) and small grain size. XRD results indicated partial oxidation of SiCN leading to formation of different yttrium silicates. No crystalline SiC or Si_3N_4 was observed. The composites' thermal properties were investigated, including heat capacity, thermal diffusivity, thermal conductivity, and coefficient of thermal expansion. The results show expected trends. Specifically:

1. For the composites, at all temperatures, the heat capacity increases as the volume fraction of SiCN increases. It also increases as temperature increases, especially at lower temperature.
2. The thermal diffusivity and conductivity of all compositions decrease with temperature and the PDC content except for the composition Y67S that is higher than that Y18S. The reason for this requires a careful phase analysis, including the volume fraction and composition of the amorphous phase.
3. The thermal expansion coefficient generally follows the rule of mixtures. At high Y_2O_3 contents, there is some deviation from the rule of mixture, most likely due to oxidation of SiCN during testing leading to higher content of yttrium silicates. The oxygen incorporation is believed to be during wet milling which was done in air environment using isopropanol.

ACKNOWLEDGMENTS

The authors would like to acknowledge support for this research from US Department of Energy, National Energy Technology Lab (award No. DE-FE003128), and GE Gas Power. This work was also supported in part by the National Science Foundation EPSCoR Program under NSF Award # OIA-1655740. Any Opinions, findings and conclusions or recommendations expressed in this material

are those of the author(s) and do not necessarily reflect those of the Department of Energy or the National Science Foundation.

ORCID

Quan Li https://orcid.org/0000-0003-2120-8196
Fei Peng https://orcid.org/0000-0002-3924-9028
Ranjendra K. Bordia https://orcid.org/0000-0001-9256-0301

REFERENCES

1. Colombo P, Raj R, Singh M, editors. Advances in polymer derived ceramics and composites. Westerville, Ohio: Wiley-American Ceramic Society; 2010.
2. Colombo P, Mera G, Riedel R, Soraru GD. Polymer-derived ceramics: 40 years of research and innovation in advanced ceramics. Ceram Sci Technol. 2013;4:245–320.
3. Greil P. Polymer derived engineering ceramics. Adv Eng Mater. 2000;2(6):339–48.
4. Yan J, Wang A, Kim D-P. Preparation of ordered mesoporous SiCN ceramics with large surface area and high thermal stability. Microporous Mesoporous Mater. 2007;100(1–3):128–33.
5. Chen CW, Huang CC, Lin YY, Chen LC, Chen KH, Su WF. Optical properties and photoconductivity of amorphous silicon carbon nitride thin film and its application for UV detection. Diamond Relat Mater. 2005;14(3–7):1010–3.
6. Liew L-A, Zhang W, Bright VM, An L, Dunn ML, Raj R. Fabrication of SiCN ceramic MEMS using injectable polymer-precursor technique. Sens Actuators A. 2001;89(1–2):64–70.
7. Li Q, Yin X, Duan W, Hao B, Kong L, Liu X. Dielectric and microwave absorption properties of polymer derived SiCN ceramics annealed in N_2 atmosphere. J Eur Ceram Soc. 2014;34(3):589–98.
8. Mera G, Tamayo A, Nguyen H, Sen S, Riedel R. Nanodomain structure of carbon-rich silicon carbonitride polymer-derived ceramics. J Am Ceram Soc. 2010;93(4):1169–75.
9. Spitsberg I, Steibel J. Thermal and environmental barrier coatings for SiC/SiC CMCs in aircraft engine applications*. Int J Appl Ceram Technol. 2005;1(4):291–301.
10. Lee KN. Environmental barrier coatings for SiC_f/SiC. Ceram Matrix Compos. 2014:430–51.
11. Günthner M, Wang K, Bordia RK, Motz G. Conversion behavior and resulting mechanical properties of polysilazane-based coatings. J Eur Ceram Soc. 2012;32(9):1883–92.
12. Greil P. Active-filler-controlled pyrolysis of preceramic polymers. J Am Ceram Soc. 1995;78(4):835–48.
13. Barroso G, Li Q, Bordia RK, Motz G. Polymeric and ceramic silicon-based coatings–a review. J Mater Chem A. 2019;7(5):1936–63.
14. Greil P, Seibold M. Modelling of dimensional changes during polymer-ceramic conversion for bulk component fabrication. J Mater Sci. 1992;27(4):1053–60.
15. Greil P. Near net shape manufacturing of polymer derived ceramics. J Eur Ceram Soc. 1998;18(13):1905–14.
16. Günthner M, Schütz A, Glatzel U, Wang K, Bordia RK, Greißl O, et al. High performance environmental barrier coatings, Part I: Passive filler loaded SiCN system for steel. J Eur Ceram Soc. 2011;31(15):3003–10.
17. Wang K, Günthner M, Motz G, Bordia RK. High performance environmental barrier coatings, Part II: Active filler loaded SiOC system for superalloys. J Eur Ceram Soc. 2011;31(15):3011–20.
18. Wang K, Unger J, Torrey JD, Flinn BD, Bordia RK. Corrosion resistant polymer derived ceramic composite environmental barrier coatings. J Eur Ceram Soc. 2014;34(15):3597–606.
19. Smokovych I, Gatzen C, Krüger M, Schwidder M, Scheffler M. Polymer derived ceramics from Si, B, SiB_6, and Mo_5SiB_2 filler-loaded perhydropolysilazane precursors as protective and functional coatings for refractory metal alloys. Materials. 2020;13(21):4878.
20. Bawane K, Lu K, Li Q, Bordia R. High temperature oxidation behaviors of SiON coated AISI 441 in Ar^+ O_2, Ar^+ H_2O, and Ar^+ CO_2 atmospheres. Corros Sci. 2020;166:108429.
21. Liu J, Zhang L, Hu F, Yang J, Cheng L, Wang Y. Polymer-derived yttrium silicate coatings on 2D C/SiC composites. J Eur Ceram Soc. 2013;33:433–9.
22. Lenz Leite M, Barroso G, Parchovianský M, Galusek D, Ionescu E, Krenkel W, et al. Synthesis and characterization of yttrium and ytterbium silicates from their oxides and an oligosilazane by the PDC route for coating applications to protect Si_3N_4 in hot gas environments. J Eur Ceram Soc. 2017;37:5177–91.
23. Webster JD, Westwood ME, Hayes FH, Day RJ, Taylor R, Duran A, et al. Oxidation protection coatings for C/SiC based on yttrium silicate. J Eur Ceram Soc. 1998;18(16):2345–50.
24. Lee KN, Fox DS, Bansal NP. Rare earth silicate environmental barrier coatings for SiC/SiC composites and Si_3N_4 ceramics. J Eur Ceram Soc. 2005;25(10):1705–15.
25. Arnal S, Fourcade S, Mauvy F, Rebillat F. Design of a new yttrium silicate Environmental Barrier Coating (EBC) based on the relationship between microstructure, transport properties and protection efficiency. J Eur Ceram Soc. 2022;42(3):1061–76.
26. Ogura Y, Kondo M, Morimoto T, Notomi A, Sekigawa T. Oxygen permeability of Y_2SiO_5. Mater Trans. 2001;42(6):1124–30.
27. Barrios E, Zhai L. A review of the evolution of the nanostructure of SiCN and SiOC polymer derived ceramics and the impact on mechanical properties. Mol Syst Des Eng. 2020;5(10):1606–41.
28. Desmaison-Brut M, Montintin J, Valin F, Boncoeur M. Influence of processing conditions on the microstructure and mechanical properties of sintered yttrium oxides. J Am Ceram Soc. 1995;78(3):716–22.
29. Bordia RK, Kang S-JL, Olevsky EA. Current understanding and future research directions at the onset of the next century of sintering science and technology. J Am Ceram Soc. 2017;100(6):2314–52.
30. Guillon O, Gonzalez-Julian J, Dargatz B, Kessel T, Schierning G, Räthel J, et al. Field-assisted sintering technology/spark plasma sintering: mechanisms, materials, and technology developments. Adv Eng Mater. 2014 16(7):830–49.
31. Olevsky E, Dudina D. Field-assisted sintering: science and applications. New York: Springer International Publishing; 2018.
32. Becker M, Shomrat N, Tsur Y. Recent advances in mechanism research and methods for electric-field-assisted sintering of ceramics. Adv Mater. 2018;30(41):1706369.
33. Chaim R, Kalina M, Shen JZ. Transparent yttrium aluminum garnet (YAG) ceramics by spark plasma sintering. J Eur Ceram Soc. 2007;27(11):3331–7.

34. Esfehanian M, Oberacker R, Fett T, Hoffmann MJ. Development of dense filler-free polymer-derived SiOC ceramics by field-assisted sintering. J Am Ceram Soc. 2008;91(11):3803–5.
35. Askeland DR, Phule PP. The science and engineering of materials. Monterey, CA: Cole Engineering Division; 1984.
36. Kroll P. Structure and reactivity of amorphous silicon nitride investigated with density-functional methods. J Non-Cryst Solids. 2001;293–295:238–43.
37. Heera V, Prokert F, Schell N, Seifarth H, Fukarek W, Voelskow M, et al. Density and structural changes in SiC after amorphization and annealing. Appl Phys Lett. 1997;70(26):3531–3.
38. Golczewski JA, Aldinger F. Thermodynamic modeling of amorphous Si–C–N ceramics derived from polymer precursors. J Non-Cryst Solids. 2004;347(1–3):204–10.
39. Thiyagarajan TK, Sreekumar KP, Selvan V, Ramachandran K, Ananthapadmanabhan PV. Simulation studies to optimize the process of plasma spray deposition of yttrium oxide. J Phys Conf Ser. 2010;208:012116.
40. Harris DC, Cambrea LR, Johnson LF, Seaver RT, Baronowski M, Gentilman R, et al. Properties of an Infrared-Transparent MgO:Y_2O_3 nanocomposite. J Am Ceram Soc. 2013;96(12):3828–35.
41. Stecura S, Campbell WJ. Thermal expansion and phase inversion of rare-earth oxides. vol. 5847. Washington: US Department of the Interior, Bureau of Mines; 1961.
42. Kumar AS, Durai AR, Sornakumar T. Yttria ceramics: cutting tool application. Mater Lett. 2004;58(11):1808–10.
43. Yoshida H, Morita K, Kim B-N, Hiraga K, Yamanaka K, Soga K, et al. Low-temperature spark plasma sintering of yttria ceramics with ultrafine grain size. J Am Ceram Soc. 2011;94(10):3301–7.
44. Duan RG, Roebben G, Vleugels J, Van der Biest O. Stability of intergranular phases in hot-pressed Si_3N_4 studied with mechanical spectroscopy and in-situ high-temperature XRD. J Eur Ceram Soc. 2002;22(11):1897–904.
45. Wan J, Gasch MJ, Mukherjee AK. Silicon nitride-silicon carbide nanocomposites fabricated by electric-field-assisted sintering. J Am Ceram Soc. 2003;86(3):526–8.
46. Wan J, Duan R, Mukherjee A. Spark plasma sintering of silicon nitride/silicon carbide nanocomposites with reduced additive amounts. Scr Mater. 2005;53(6):663–7.
47. Munir ZA, Anselmi-Tamburini U, Ohyanagi M. The effect of electric field and pressure on the synthesis and consolidation of materials: a review of the spark plasma sintering method. J Mater Sci. 2006;41:763–77.
48. An L, Ito A, Goto T. Transparent yttria produced by spark plasma sintering at moderate temperature and pressure profiles. J Eur Ceram Soc. 2012;32(5):1035–40.
49. Wills RR, Cunningham JA, Wimmer JM, Stewart RW. Stability of the silicon yttrium oxynitrides. J Am Ceram Soc. 1976;59(5–6):269–70.
50. Sun Z, Li M, Zhou Y. Recent progress on synthesis, multiscale structure, and properties of Y–Si–O oxides. Int Mater Rev. 2014;59(7):357–83.
51. Tritt TM, Weston D. Measurement techniques and considerations for determining thermal conductivity of bulk materials. Thermal conductivity. Physics of solids and liquids. Boston, MA: Springer; 2004. p. 187–203.
52. Sun Z, Li M, Zhou Y. Thermal properties of single-phase Y_2SiO_5. J Eur Ceram Soc. 2009;29(4):551–7.
53. Tian Z, Zheng L, Li Z, Li J, Wang J. Exploration of the low thermal conductivities of γ-$Y_2Si_2O_7$, β-$Y_2Si_2O_7$, β-$Yb_2Si_2O_7$, and β-$Lu_2Si_2O_7$ as novel environmental barrier coating candidates. J Eur Ceram Soc. 2016;36(11):2813–23.
54. Wingert MC, Zheng J, Kwon S, Chen R. Thermal transport in amorphous materials: a review. Semicond Sci Technol. 2016;31(11):113003.

How to cite this article: Zhang Z, Li Q, Maiti SC, Shen X, He J, Peng F, et al. Thermal properties of field-assisted-sintered SiCN–Y_2O_3 composites. Int J Appl Ceram Technol. 2023;20:1060–1070. https://doi.org/10.1111/ijac.14265